

# The mechanism of non-blocking inhibition of sodium channels revealed by conformation-selective photolabeling

Mátyás Földi<sup>1</sup>, Krisztina Pesti<sup>2</sup>, Katalin Zboray<sup>1</sup>, Adam Toth<sup>1</sup>, Tamás Hegedűs<sup>3</sup>, András Málnási-Csizmadia<sup>2</sup>, Peter Lukacs<sup>1</sup>, and Arpad Mike<sup>1</sup>

<sup>1</sup>Centre for Agricultural Research

<sup>2</sup>Eötvös Loránd University

<sup>3</sup>Semmelweis University

July 29, 2020

## Abstract

Hyperexcitability-related diseases include epilepsies, pain syndromes, neuromuscular disorders, and cardiac arrhythmias. Sodium channel inhibitors can be used to treat these conditions, however, their applicability is limited by their nonspecific effect on physiological function. They act by channel block (obstructing ion conduction, since the binding site is within the channel pore), and by modulation (delaying recovery from the non-conducting inactivated state). Channel block inhibits healthy and pathological tissue equally, while modulation can preferentially inhibit pathological activity. Therefore, an ideal sodium channel inhibitor drug would act by modulation alone. Unfortunately, thus far no such drug has been known to exist. Here we present evidence that riluzole acts by this “ideal” mechanism, “non-blocking modulation” (NBM). We propose that, being a relatively small molecule, riluzole is able to stay bound to the binding site, but nonetheless stay off the conduction pathway, by residing in one of the “fenestrations” (cavities connecting the central cavity to the membrane phase). Using precisely timed UV pulses to photolabel specific conformations of the channel, we show that association to the local anesthetic binding site requires prior inactivation. We discuss why kinetics of binding is crucial for selective inhibition of pathological activity, and how the NBM mechanism can be recognized using a special voltage- and drug application-protocol. Our results identify riluzole as the prototype of this new class of sodium channel inhibitors. Drugs of this class are expected to selectively prevent hyperexcitability, while having minimal effect on cells firing at a normal rate from a normal resting potential.

## KEYWORDS

sodium channels, riluzole, local anesthetics, binding sites, epilepsy, pain, arrhythmias

## BULLET POINT SUMMARY:

### What is already known

- Sodium channel inhibitors act by channel block.
- A ligand can either have high affinity, or fast onset/offset kinetics, but cannot have both.

### What this study adds

- Binding site occupancy in sodium channels does not necessarily mean inhibition. Non-blocking modulation is possible.
- This mechanism enables riluzole to have both fast onset/offset kinetics and high affinity.

### Clinical significance

- Non-blocking modulation is especially effective against hyperexcitability conditions and pathological high frequency firing.
- Compounds of this class may be superior antiepileptics, analgesics, antiarrhythmics, or neuroprotectants.

## 1 INTRODUCTION

Hyperexcitability is at the core of a rather diverse set of disorders affecting the heart, skeletal muscles, and the nervous system. Out-of-control electric activity is involved in the development of several types of epilepsies, chronic pain syndromes, neuromuscular disorders, cardiac arrhythmias, and even psychiatric disorders (Rogawski & Löscher, 2004). These conditions can originate from genetic conditions (mutations altering the operation of channels themselves, or proteins involved in their modulation), or can be due to damages caused by mechanical injury, inflammation or ischemia.

To suppress hyperexcitability, sodium channels are the primary target because they are responsible for the fast onset of action potentials, as well as their all-or-none and self-regenerating nature. A small fraction (0.5 to 5%) of sodium channels evades rapid inactivation and produces a current component named persistent or late sodium current. This component plays a crucial role in the initiation of action potentials, and its enlargement has been observed in several hyperexcitability-related pathologies (Cannon, 2018; Lampert et al., 2006; Makielski, 2016; Meisler, 2019; Stafstrom, 2007; Tang et al., 2015; van Zundert et al., 2012).

In order to design therapeutically useful sodium channel inhibitors, one encounters the seemingly impossible task of having to prevent pathological hyperexcitability, while maintaining the normal physiological activity of nerves and muscles. Interestingly, there are compounds, which are able to carry out this feat – at least to a certain extent. These compounds include antiarrhythmic, antiepileptic, antispastic, etc. compounds. The trick that enables them to do so is state-dependence, i.e., their preference for certain conformational states of the channel protein. Most sodium channel inhibitors prefer inactivated state to resting state, they bind to it more rapidly, and/or dissociate from it more slowly. The fact that an inhibitor has a higher affinity to inactivated state, means that drug-bound inactivated channels form an energetically favorable complex. This implies both slower dissociation of the ligand from this conformation and slower recovery from inactivated to resting state. The latter effect – called modulation of channel gating – is an inseparable element of state-dependent inhibition, as described by the modulated receptor hypothesis (Hille, 1977). High affinity to inactivated state ensures delayed dissociation, while modulation ensures delayed conformational transition to the low affinity resting state, thus restraining both possible pathways to recovery (dissociation followed by recovery, or recovery followed by dissociation).

Pathological states induced by injury, inflammation, ischemia, tumor, or epilepsy alter the electrical characteristics of excitable cells, which may include a depolarized membrane potential due to energy failure, increased leakage currents, left-shifted voltage sensitivity of sodium channels, and increased persistent component of the sodium current (Fischer et al., 2017; Hammarström & Gage, 2002; Ma et al., 2006; Morris & Joos, 2016; Q. Zhang et al., 2019; Zheng et al., 2012). These changes make sodium channels more likely to be in open and inactivated conformations, therefore state-selectivity alone is enough for preferential inhibition of pathological tissue. On a first impression, one could suppose that the stronger the state-preference is, the better the drug will be.

However, the temporal aspect must also be considered. Action potentials are fired repetitively, and pathological behavior of neurons is often manifested as high-frequency firing. The extent of state-dependence is, therefore, not the only crucial aspect, equally important is the onset/offset dynamics of state-dependent binding. Its significance is obvious in the case of Class 1 antiarrhythmics, where subclasses a, b, and c differ in their association/dissociation kinetics, but the same is true for the much higher firing rates in central and peripheral neurons. For selective inhibition of cells firing at pathologically high frequency, the ideal drug should work as a low pass filter, with a steep frequency response, to be able to distinguish pathological and physiological rates of firing. This, however, presents a theoretical limit for state-dependent binding, because fast dissociation precludes high affinity. One would want both fast binding/unbinding dynamics, and high

state dependence. However, high state-dependence requires high affinity to inactivated state, and high affinity means slow dissociation, which means that binding/unbinding dynamics cannot be fast.

Intriguingly, riluzole seems to be able to elude this limitation. Here we examine how this is possible.

We first describe the peculiar pattern of inhibition, we observed during and after riluzole perfusion. We use a voltage-clamp protocol where block and modulation of the channels are monitored in parallel. Paradoxically, two distinct recovery processes seem to coexist, with rates differing by more than two orders of magnitude. We presume that this peculiarity may be the key to being able to feature fast kinetics and high affinity at the same time. A fast recovery allows channels to regain their ability to conduct ions within  $\sim 10$  ms. In spite of their ability to conduct, however, channels remain modulated by the drug for a much longer time: it requires  $\sim 2$  s for the channels to recover from the modulatory influence. This mechanism enables riluzole to function as a low pass filter with an exceptionally steep frequency response, which is probably a key element of its distinctive therapeutic efficacy.

We set out to identify the physical processes that underlie fast and slow recovery processes with the help of conformation-selective photolabeling-coupled electrophysiology, and in silico docking experiments.

## 2 METHODS

### 2.1 Cell culture and expression of recombinant sodium channels

Cloning of the wild type and F1579A mutant rNav1.4 channel constructs was performed as described previously (Lukacs et al., 2018).

Recombinant sodium channel-expressing cell lines were generated by transfection of wild type and F1579A mutant Nav1.4 BAC DNA constructs into HEK 293 cells (ATCC CRL-1573) by Fugene HD (Promega, Fitchburg, WI) transfection reagent according to the manufacturer's recommendations. Cell clones with stable vector DNA integration were selected by the addition of Geneticin (Life Technologies, Carlsbad, CA) antibiotic to the culture media (400 mg/ml) for 14 days. HEK293 cells were maintained in Dulbecco's Modified Eagle Medium, high glucose supplemented with 10% v/v fetal bovine serum, 100 U/ml of penicillin/streptomycin and 0.4 mg/mL Geneticin (Life Technologies, Carlsbad, CA). For experiments cells were plated onto 35-mm Petri dishes or T75 flasks, and cultured for 24–36 h. For manual patch-clamp experiments, Petri dishes were transferred to the recording chamber, where cells were kept under continuous flow of extracellular solution. For Port-a-Patch experiments, cells were dissociated from the dish with trypsin-EDTA, centrifuged, and suspended into the extracellular solution.

### 2.2 Electrophysiology

The composition of solutions (in mM) was: Intracellular solution: 50 CsCl, 10 NaCl, 60 CsF, 20 EGTA, 10 HEPES; pH 7.2 (adjusted with 1 M CsOH). Extracellular solution: 140 NaCl, 4 KCl, 1 MgCl<sub>2</sub>, 2 CaCl<sub>2</sub>, 5 D-Glucose and 10 HEPES; pH 7.4 (adjusted with 1 M NaOH). The osmolality of intra- and extracellular solutions was set to  $\sim 290$  and  $\sim 300$  mOsm, respectively. Data were sampled at 20 kHz, and filtered at 10 kHz. Experiments were carried out at room temperature.

In manual patch-clamp experiments, whole-cell currents were recorded using an Axopatch 200B amplifier and the pClamp software (Molecular Devices, San Jose, CA). Pipette resistance ranged between 1.5 and 4.0 M $\Omega$ . Solution exchange was performed by the "liquid filament switch" method (Franke et al., 1987; Jonas, 1995), using a Burleigh LSS-3200 ultrafast solution switching system, as described in detail previously (Pesti et al., 2014). The flow rate was set using a DAD-12 solution exchange system (ALA Scientific Instruments Inc., Farmingdale, NY), to 0.2-0.3 ml/min, which corresponded to 5-20 cm/s velocity. Ten to 90% solution exchange rates were between 1 and 3 ms.

In experiments with the Port-a-Patch system (Nanion, Munich, Germany) currents were recorded using an EPC10 plus amplifier, and the PatchMaster software (HEKA Electronic, Lambrecht, Germany). During cell catching, sealing, and whole-cell formation, the PatchControl software (Nanion) commanded the amplifier and the pressure control unit. The resistance of borosilicate chips was 2.0–3.5 M.

## 2.3 Voltage protocols

The "steady-state inactivation" (**SSI**) protocol investigated the availability of channels at different membrane potentials, the "recovery from inactivation" (**RFI**) protocol investigated the dynamics of channels regaining their availability after inactivation, and the state-dependent onset (**SDO**) protocol investigated the dynamics of developing inhibition. These same protocols have been used before (Lukacs et al., 2018); and they are illustrated in Fig. 5A.

The "three pulse train" (**3PT**) protocol (Fig. 2A and D) was similar to the one we called by this name before (Lukacs et al., 2018); but in this study, it was optimized for maximal time resolution. The protocol is designed to monitor changes in both gating kinetics and gating equilibrium. For the sake of high time resolution, it uses only a single interpulse interval: 2 ms (instead of several interpulse intervals as in **RFI**), and only a single membrane potential: -65 mV (instead of several membrane potentials as in the "steady-state inactivation" protocol – **SSI**). Thus we could record changes at 26 ms resolution (38.5 Hz). In each experiment, we delivered 100 consecutive trains: after 6 initial control trains we perfused riluzole throughout 10 trains (i.e., for 260 ms), and then monitored washout for the remaining 84 trains. Perfusion was started and stopped during the 10 ms intervals between two trains, which was amply enough for complete exchange of the solution with the theta tube system.

Peak amplitudes of evoked currents have been determined after subtracting capacitive and leakage artifacts. Recordings from a typical cell throughout a 100 train experiment are shown in Fig. 2B. The 6 control traces are shown in blue, the 10 traces recorded during riluzole perfusion are in red (dark to light red indicates consecutive traces), and currents evoked during washout are shown in light gray to black. Fig. 2C illustrates the same currents after subtraction of artifacts. Fig. 2D shows the same corrected current traces are shown in sequential order, together with the voltage protocol, as they were evoked in the experiment (only the first 29 of the 100 trains, for the sake of clarity). Peak amplitudes are marked by circles: blue (1<sup>st</sup> pulses), red (2<sup>nd</sup> pulses), and green (3<sup>rd</sup> pulses). Connecting blue, red, and green circles we get different onset and offset characteristics, as shown for  $n = 7$  cells in Fig. 2E. All amplitudes were normalized to the 1<sup>st</sup> pulse-evoked amplitude at the start of the experiment (1<sup>st</sup>, 2<sup>nd</sup>, and 3<sup>rd</sup> pulse-evoked amplitudes each to its own control, to help comparison of inhibited fractions). Current traces for the same seven cells, as well as for the nine recorded binding site mutant cells are shown in supporting information Fig. S1, together with a detailed discussion of fitted time constants.

A small fraction of channels ( $11.4 \pm 0.1\%$  by the end of the 100<sup>th</sup> train) underwent slow inactivation during the test; this was a necessary tradeoff for high temporal resolution. In order to appropriately calculate the extent of inhibition by riluzole, we corrected for the slow inactivated fraction: A sum of an exponential and a linear component was fit to the first 6 and last 3 points of 1st pulse-evoked current amplitudes in each cell (supporting information Fig. S1B and H). This fitted function represented the non-slow-inactivated fraction  $f_{nsi}(t)$  of the channel population. Measured amplitude plots ( $A_M(t)$ ), then were transformed into corrected amplitude plots ( $A_C(t)$ ) by expressing it as a fraction of non-slow-inactivated channels:  $A_C(t) = A_M(t) / f_{nsi}(t)$ . This is illustrated in supporting information Fig. S1B and C, where panel C shows the same data as panel B, after correction. Measurement of the extent of inhibition and determination of onset and offset time constants were performed on the corrected plots.

## 2.4 UV photoactivation

The recording chamber of the Port-a-Patch was customized to accommodate a 400  $\mu\text{m}$  diameter quartz optic fiber, which was placed 3–4 mm (or 5–7 mm in a subset of experiments) above the recorded cell. The original perfusion manifold was replaced by a custom manifold positioned to the side of the recording chamber opposite to the waste removal. Solution exchange was complete within 1–2 s. UV light pulses were delivered by a 310 nm fiber-coupled Mightex FCS-0310-000 LED (Mightex, Pleasanton, CA), with 40  $\mu\text{W}$  intensity. Pulses were triggered by the PatchMaster software.

## 2.5 Combined voltage and illumination protocols

To perform photolabeling-coupled electrophysiology experiments, we used the photoreactive analog of riluzole, azido-riluzole (Lukacs et al., 2018). During drug perfusion, we used one of three illumination protocols, to compare the possibility of binding to different conformations (Fig. 5A). While one of the three protocols was repeated at 2.5 Hz (every 400 ms), 90 ms UV light pulses were applied within each cycle. The UV pulses were delivered either during hyperpolarizations, ("resting-state-illumination"); during depolarizations ("inactivated-state-illumination"); or while cells were kept at the approximate half-inactivation voltage ("V-half-illumination"), i.e., when channels were distributed roughly equally between the two conformations. To each cell, a maximum of 450 UV pulses was delivered (*i.e.*, for up to 3 min), it was stopped earlier whenever evoked currents were inhibited to ~20% of their original amplitude. (Note that an 80% inhibition did not mean an 80% occupancy of binding sites, as we will discuss below.) Gating kinetics and equilibrium of the channels were investigated both before drug perfusion and after washout, using the "recovery from inactivation" (**RFI**), "steady-state inactivation" (**SSI**) and "state-dependent onset" (**SDO**) voltage protocols.

Variations in the combined voltage and illumination protocols provided further insight in the mechanism, regarding the relative contribution of modulation and channel block (supporting information Fig. S2), and regarding the sequence of recovery from inactivation and unbinding (supporting information Fig. S3).

## 2.6 Data analysis

Curve fitting was done in Microsoft Excel, using the Solver Add-in. Steady-state inactivation (**SSI**) curves were fitted using the Boltzmann function:  $I = I_{max} / \{1 + \exp[(V_p - V_{1/2}) / -k]\}$ , where  $V_p$  is the pre-pulse potential,  $V_{1/2}$  is the voltage where the curve reached its midpoint, and  $k$  is the slope factor.

Recovery from inactivation (**RFI**) experiments were fitted by mono- or bi-exponential function:  $I = A_1 * [1 - \exp(-t_{ip} / \tau_1)]^n + A_2 * [1 - \exp(-t_{ip} / \tau_2)]$ , where  $\tau_1$  and  $\tau_2$  are the fast and slow time constants,  $A_1$ , and  $A_2$  are their contributions to the amplitude ( $A_2 = 0$ , for monoexponential fitting), and  $t_{ip}$  is the duration of the interpulse interval. We observed that recovery (not only in control, but in the presence of riluzole, and with covalently bound azido-riluzole as well) was steeper than a simple exponential function, therefore we introduced the exponent  $n$ . When its value was unconstrained, best fits produced  $n = 2.35 \pm 0.65$  in control (range: 1.22 to 3.15) and  $n = 3.19 \pm 0.51$  in the presence of 100  $\mu$ M riluzole (range: 1.95 to 5.54). However, the value of the exponent affected the value of the time constant, as we have discussed before (Lukacs et al., 2018). For this reason, we chosen  $n = 1.5$ , the lowest exponent that could acceptably fit our data, and used it for fitting throughout the experiments.

State-dependent onset (**SDO**) data were fitted with either single or double exponential functions:  $I = A_1 * \exp(-t_p / \tau_1) + A_2 * \exp(-t_p / \tau_2)$ , where  $A_1$  and  $A_2$  are the relative amplitudes of the two components, and  $t_p$  is the duration of the pulse.

Averaging of **SSI**, **RFI**, and **SDO** curves was not done by calculating the mean of measured points because this would introduce an error in the slope of curves. Instead, parameters from individually fitted experimental curves were averaged (arithmetic mean for amplitudes, membrane potential values, and slope factors; geometric mean for time constants), and the curve was constructed using the averaged parameters.

Apparent affinity ( $IC_{50}$ ) values were calculated from either the extent of inhibition or from the onset and offset time constants. Apparent affinity is a useful way to represent the potency of sodium channel inhibitors under specific circumstances. This potency can change radically even on the sub-millisecond time scale, as seen for example in the **3PT** protocol, depending on the temporal pattern of membrane potential, due to the interrelated dynamics of binding and gating. Apparent affinity values can be calculated from a single inhibition value, using the simplified Hill equation: when a one-to-one binding is assumed, the Hill equation is reduced to  $Inh = cc / (cc + IC_{50})$ , where  $Inh$  is the inhibited fraction and  $cc$  is the drug concentration. The calculation is most accurate at ~50% inhibition, but becomes increasingly inaccurate as inhibition approaches either 0 or 100%.

Apparent affinity can also be calculated from onset and offset time constants (obtained by single exponential

fitting of amplitudes in the **3PT** protocol), if we suppose a single-step binding reaction:  $IC_{50} = cc * \tau_{ov} / (\tau_{o\phi\phi} - \tau_{ov})$ . In the case of riluzole, as we will discuss below, the inhibited fraction and the bound fraction were not equivalent, therefore we expected that the  $IC_{50}$  values calculated by the two ways will differ (see Fig. S1 in supporting information).

## 2.7 Statistics

The data and statistical analysis comply with the recommendations of the British Journal of Pharmacology on experimental design and analysis in pharmacology (Curtis et al., 2018). All values are given as mean  $\pm$  SEM;  $n$  is the number of cells recorded from, we collected no technical replicates. Experiments with low seal resistance ( $< 1 \text{ G}\Omega$ ), high series resistance ( $> 10 \text{ M}\Omega$ ), or small currents ( $< 1 \text{ nA}$ ) were excluded from analysis. Because seal resistance or series resistance occasionally changed during experiments, group sizes varied between  $n = 6$  and  $n = 9$ . This presents no problem in statistical evaluation, since all post-treatment measurements were compared to pre-treatment measurements in the same cell, therefore group were of equal sizes in all statistical tests. The two-tailed, paired Student's t-test was used for comparing drug effects to control (in Microsoft Excel). Normalization was done after statistical evaluation, only for the sake of making observed effects comparable. In statistical tests we chose to give the exact level of significance (value of  $P$ ) rather than considering changes significant if  $P$  is less than an arbitrary value (0.05), because this gives more information regarding the magnitude and consistency of observed changes.

## 2.8 Materials

All chemicals were obtained from Sigma-Aldrich. Azido-riluzole was synthesized by SONEAS Research Ltd., Budapest, Hungary.

## 2.9 Structural models and in silico docking

The human Nav1.4 (PDB ID: 6AGF) was used, since *in silico* docking is more reliable to experimental structures than to homology models. The F1586A mutant structure was prepared manually by removing atoms of Phe and renaming the residue to Ala. The protein and riluzole (ZINC database ID: ZINC26671469) structures were prepared using `prepare_ligand4.py` and `prepare_receptor4.py` scripts from MGLTools with default options except hydrogens were added in the case of the protein (<https://ccsb.scripps.edu/mgltools>). Riluzole was docked to the wild type and F1586A mutant structures using Autodock Vina (Trott & Olson, 2010). The search space was set up in PyMOL (The PyMOL Molecular Graphics System, Version 2.4, Schrödinger, LLC.) via the Autodock/Vina plugin (Seeliger & de Groot, 2010) (supporting information Fig. S4). The exhaustiveness option of Vina was set 128 instead of the default 8 for increasing the probability of finding the minimum of the scoring function. The `num_modes` and `energy_range` options were set to 100 and 20, respectively, to output a higher number of docked poses.

## 2.10 Nomenclature of targets and ligands

Key protein targets and ligands in this article are hyperlinked to corresponding entries in <http://www.guidetopharmacology.org>, the common portal for data from the IUPHAR/BPS Guide to PHARMACOLOGY (Armstrong et al., 2019) and are permanently archived in the Concise Guide to PHARMACOLOGY 2019/20 (Alexander et al., 2019).

## 3 RESULTS

### 3.1 Fast recovery in the presence of the drug.

Results of the **RFI** experiment in control and in the presence of 100  $\mu\text{M}$  riluzole are illustrated in Fig. 1. In general, sodium channel inhibitor drugs are most effective at short hyperpolarizing gaps, and their inhibitory effect gradually decreases with longer hyperpolarizations. This is conventionally explained by the progressive dissociation of drug molecules from resting state throughout the hyperpolarizing period because they have lower affinity to resting than to inactivated state. In the absence of any drug, at  $-130 \text{ mV}$  channels recovered with a time constant of  $0.39 \pm 0.08 \text{ ms}$  (exponentials on the 3<sup>rd</sup> power, see Methods). In the presence of 100

$\mu\text{M}$  riluzole recovery was delayed, it proceeded with a time constant of  $2.25 \pm 0.004$  ms ( $p = 0.00012$ , paired t-test,  $n = 9$ ). Does this time constant indeed reflect dissociation?

### 3.2 Fast and slow recovery upon removal of the drug.

We investigated the onset and offset kinetics using the **3PT** protocol (Fig. 2, see Methods for the details of the protocol). The offset of inhibition upon actual removal of the drug was more than hundredfold slower than recovery from inactivation in the presence of riluzole: it occurred with a time constant of  $824 \pm 99$  ms (Fig. 2F). Paradoxically, within each cycle, the recovery was almost complete within each 10 ms of between-trains hyperpolarization (see the minimal inhibition at blue traces), but then the inhibition was reestablished before the 2<sup>nd</sup> depolarization, and became even stronger during the subsequent 8 ms spent near the  $V_{1/2}$  (-65 mV), causing a massive inhibition at the 3<sup>rd</sup> pulse of each train. This pattern repeated itself during riluzole perfusion, and also for 1-2 s after riluzole had been washed out.

The extent of inhibition in 1<sup>st</sup>, 2<sup>nd</sup>, and 3<sup>rd</sup> pulse-evoked currents was  $16.1 \pm 4.0\%$ ,  $73.4 \pm 3.9\%$ , and  $95.4 \pm 1.2\%$ . Apparent affinity ( $IC_{50}$ ) values can be determined from the extent of inhibition, as described in Methods; these values corresponded with  $606 \pm 137$   $\mu\text{M}$ ,  $33.5 \pm 6.8$   $\mu\text{M}$ , and  $3.98 \pm 1.32$   $\mu\text{M}$ , respectively. Mean  $\pm$  SEM of time constants for the 7 cells are shown in Fig. 2F.

In conclusion, two distinct recovery processes coexisted with completely different kinetics. Recovery is conventionally explained by dissociation, but the two recovery processes with more than hundredfold different time constants obviously cannot both reflect dissociation. To investigate what physical processes underlie the progression of both fast and slow recovery, we first studied the effect of mutating the most important residue of the local anesthetic binding site, F1579. The presence of this aromatic residue is crucial in determining the affinity of binding (Mike & Lukacs, 2010; Zhang et al., 2015), and also in coupling drug binding to altered voltage sensor movements (Hanck et al., 2009; Muroi & Chanda, 2009), which is the basis of gating modulation.

### 3.3 The two recovery processes in binding site mutant channels.

We repeated the same experiments using the **RFI** and **3PT** protocols in cells expressing binding site mutant (F1579A) channels. We found that both the fast and the slow processes were radically altered by the mutation. In mutant channels fitting the recovery required a biexponential function, the major fast component had a time constant of  $0.30 \pm 0.02$  ms, and it contributed  $85.5 \pm 2.5\%$  to the amplitude. The time constant of the minor, slow component was  $4.36 \pm 0.62$  ms. Riluzole only slightly delayed fast component, to  $0.43 \pm 0.02$  ms ( $p = 0.012$ , paired t-test,  $n = 7$ ) (Fig. 3). The minor, slow component was not changed significantly.

The effect of the mutation on the fast recovery was also indicated by the decreased inhibition of 2<sup>nd</sup> pulse-evoked currents in the **3PT** protocol (Fig. 4), see the minimal difference between blue and red traces in Fig. 4D. Interestingly, 3<sup>rd</sup> pulse-evoked currents were still considerably inhibited (by  $37.2 \pm 6.6\%$ ). Apparent affinity ( $IC_{50}$ ) values, calculated from the extent of inhibition, were  $1590 \pm 180$   $\mu\text{M}$ ,  $895 \pm 126$   $\mu\text{M}$ , and  $114 \pm 20.0$   $\mu\text{M}$  for 1<sup>st</sup>, 2<sup>nd</sup>, and 3<sup>rd</sup> pulse-evoked currents, respectively. Compared to the apparent affinity values of WT channels, 1<sup>st</sup> pulse-evoked responses were least sensitive to the mutation (2.62-fold decrease in affinity;  $p = 0.012$ , paired t-test,  $n = 9$ ), while 2<sup>nd</sup> and 3<sup>rd</sup> pulse-evoked responses much more sensitive (26.7-fold and 28.6-fold decrease in affinity, respectively;  $p < 1 \cdot 10^{-7}$  for both).

The slow recovery process was also accelerated, (compare Fig. 4E to Fig. 2F). For a detailed analysis of time constants see supporting information Fig. S1.

### 3.4 Conformation-selective photolabeling. The problem of interrelated binding and gating .

To summarize, we observed two distinct recovery processes, and they were both accelerated by mutation of the local anesthetic binding site. What physical processes may underlie them?

In the presence of riluzole, the rate of the fast recovery process may be determined either by modulated gating (i.e., recovery from inactivation is slowed down by the bound drug) or by the dissociation of the drug – which is the conventional explanation.

The modulated receptor hypothesis (Hille, 1977) predicts that, since the drug has different affinities to different conformational states, drug binding must alter the energetics of conformational transitions, making higher affinity states more stable. Any mutation that changes binding affinities to different states must also change the effect of the drug on rates of transitions between these states (i.e., the gating of drug-bound channels). In other words, decreased affinity must necessarily cause decreased modulation of gating. Mutation-induced changes in the fast and slow recovery processes, therefore, could both be manifestations of decreased affinity, on the level of gating and binding, respectively. Mutation-induced acceleration of the fast recovery process (compare Fig. 1 and Fig. 3) may be due to decreased modulation of channel gating, while acceleration of the slow recovery process (compare Fig. 2F and 4E) may be caused (at least partly) by faster ligand unbinding. If we accept this explanation, we must suppose that channel gating alone (without dissociation of the inhibitor) can make the channel available for activation and conduction, in other words, drug-bound channels can conduct, therefore "non-blocking modulation" (Lukacs et al., 2018) is possible.

The complex problem of interrelated gating and binding/unbinding can be simplified using photolabeling-coupled electrophysiology, as we have previously demonstrated (Lukacs et al., 2018). By binding the photoreactive riluzole analog, azido-riluzole, covalently to the channel, we could exclude the processes of binding and unbinding. We found that covalently bound channels were still able to conduct ions, but with modulated gating. In the **3PT** protocol modulated gating was reflected as the difference between 1<sup>st</sup> and 2<sup>nd</sup> pulse-evoked currents (Fig. 2). This difference almost disappeared when the key residue of the local anesthetic binding site was mutated (Fig. 4). It was logical to investigate if mutation of the same residue would cause the same lack of modulation in photolabeling-coupled electrophysiology experiments. In addition, we also investigated whether the binding was conformation-dependent. We have improved the method of photolabeling-coupled electrophysiology by synchronizing UV light pulses with the voltage protocol, instead of the continuous illumination we had used previously (Lukacs et al., 2018). This allowed us to target specific conformations of the channel, and also to verify that the channel-ligand complex indeed assumes a drug-bound resting conformation before unbinding occurs. By precise timing of the UV light pulse, it was possible to test how soon this unfavorable drug-bound resting conformation was ended by unbinding (see supporting information). These data helped us identify the physical processes underlying both fast and slow recovery processes.

### 3.5 State-dependence of binding.

Riluzole, like most sodium channel inhibitors, is known to preferentially bind to inactivated channels (Catterall et al., 2019). We first intended to investigate how the conformation of the channel influences the ability of the drug to bind. We used the three voltage and illumination protocols as described in Methods. Before drug perfusion and after washout we assessed changes in gating kinetics and equilibrium of the channels by using the **RFI**, **SSI**, and **SDO** voltage protocols. Covalent binding-induced changes in channel gating kinetics (**RFI** and **SDO**) and gating equilibrium (**SSI**) are shown in Fig. 5B, C, D. Blue, teal, and green colors indicate resting-state-, V-half-, and inactivated-state-illumination, respectively. Insets show normalized data, where amplitudes were normalized to the maximal amplitude after azido-riluzole perfusion and irradiation. This gives a clearer picture of how the gating has been modulated. Similarly to our earlier data (Lukacs et al., 2018) obtained using continuous illumination, the population of ion channels that were still conducting showed modulated gating: delayed recovery from inactivation (Fig. 5B), shifted steady-state availability (Fig. 5C), and accelerated onset of inhibition (Fig. 5D). Note that the **SDO** curves were also affected by covalently bound ligand; in the case of the inactivated-state-illumination protocol, the onset proceeded with a time constant of  $1.21 \pm 0.12$  ms. Since there was no possibility of binding or unbinding, this must correspond with a conformational rearrangement of the ligand-channel complex.

Interestingly, 90 ms UV pulses delivered at every 400 ms during inactivated conformation were as effective as continuous illumination had been (Lukacs et al., 2018), in spite of the fact that the total illumination time was only 23.75% of it. It seems that repeatedly allowing azido-riluzole molecules to diffuse to their most favorable location (probably the binding site) without activating them, and then delivering the UV pulse only when they are at the right location, actually works as effectively as continuous illumination.

In contrast, when UV pulses were delivered during resting state, no significant decrease of current amplitudes was observed, and changes in recovery kinetics (**RFI** protocol) and equilibrium of inactivation (**SSI** protocol) were also non-significant ( $p = 0.2$  and  $p = 0.25$  for changes in the predominant time constant of recovery and  $V_{1/2}$ , respectively,  $n = 7$ ). This may either suggest that the central cavity or the binding site itself is inaccessible at resting conformation, or that the binding site has very low affinity at resting state. UV pulses delivered at the approximate half-inactivation voltage were between the other two illumination protocols in effectiveness.

### 3.6 The specificity of binding.

Next, we investigated how specific the binding was, by testing the F1579A binding site mutant channels. We expected that if the binding was indeed specific, then we would see neither inhibition of the amplitude nor modulation of gating. Interestingly, mutation of the binding site did not prevent inhibition of the amplitude (provided that channels assumed inactivated conformation), but the modulation of gating was radically decreased (Fig. 6A, B, C). This suggests that when the high-affinity binding site is disrupted, inhibition is still possible, probably by binding to secondary binding sites, but these binding sites are less potent in conferring gating modulation. The involvement of this phenylalanine in the mechanism of modulation has been shown before (Ahern et al., 2008; Arcisio-Miranda et al., 2010; Hanck et al., 1994; Hanck et al., 2009; Liu et al., 2003; Muroi & Chanda, 2009), therefore the lack of significant modulation is not unexpected. However, the fact that mutant channels could still be effectively inhibited in inactivated state, was indeed unexpected, and it suggests the existence of one or more additional binding sites. Association to these lower affinity binding sites, which too were only available in the inactivated conformation, caused predominantly channel block, and less modulation.

### 3.7 Possible location of bound riluzole.

To gain insights into the possible binding sites of riluzole, we performed *in silico* docking of this small molecule to the wild type and mutant Nav1.4 structures. The human Nav1.4 (PDB ID: 6AGF) was used, since *in silico* docking is more reliable to experimental structures than to homology models. Importantly, riluzole binding was not observed in the pore region or close to the pore in the central cavity in either the wild type or the F1586A (F1579A in rNav1.4) structures (Fig. 7). This inhibitor bound among transmembrane helices in three fenestrations of the wild type structure. In all cases, interactions involved the aromatic side chain of phenylalanine residues (F436, F1284, and F1586; which correspond to F430, F1277, and F1579 in rNav1.4), which are shown in Fig. 7. In the absence of the phenylalanine side chain in the F1586A mutant, only two binding sites were observed at F436 and F1284.

## 4. DISCUSSION

Our data suggest that riluzole is the first member of an entirely new class of sodium channel inhibitor compounds. Its primary binding site is the well-characterized "local anesthetic receptor," with F1579 as the key residue. However, the location of the bound ligand is different from that of local anesthetics, and the effect exerted by it is also radically different. As for the location, *in silico* docking revealed that unlike other sodium channel inhibitor molecules, riluzole was preferentially located within the fenestrations, and tended to avoid the central part of the pore or the vicinity of the selectivity filter, where it could interfere with conduction. Localization within the fenestration has been previously observed in molecular dynamics simulations investigating the general anesthetic isoflurane (Raju et al., 2013) and propofol (Wang et al., 2018), as well as the local anesthetic benzocaine (Boiteux et al., 2014; Buyan et al., 2018; Martin & Corry, 2014) and lidocaine (neutral form) (Nguyen et al., 2019), but it has never been found to be the dominant position. The unusual location predicted by *in silico* docking is supported by the way riluzole acted in experiments. It stabilized inactivated conformation without interference with conduction. Inactivated state stabilization affected both the equilibrium and the recovery rate, as evidenced by the shift of the **SSI** and the **RFI** curves, respectively (Fig. 1; see also Fig. 1 in (Lukacs et al., 2018)).

The non-instantaneous onset (as seen in the **SDO** protocol) and the delayed recovery (see the **RFI** protocol) together ensure that effective inhibition is confined within a strict temporal window. Single pulse-evoked

currents or synaptic activity-evoked action potentials are "missed" by riluzole because inhibition becomes effective only after the channel has reached inactivated conformation, and the conformation of the ligand-channel complex has been stabilized. After this, the inhibition is effective, but only for a limited time – even in the case of the non-therapeutic concentration of 100  $\mu\text{M}$  it was only effective for approximately 10-20 ms. At therapeutic concentrations the effect of riluzole is no more than a fine modulation: the refractory time after an action potential is prolonged by a few milliseconds, and a small fraction of the channel population is kept in inactivated conformation. The exact extent of prolongation and the magnitude of the fraction kept in inactivated conformation is dependent on the membrane potential during the interspike interval. This temporal window of effectiveness is the basis of both persistent (or "late") sodium current selectivity and the low pass filtering effect. The contribution of the persistent component of sodium currents ( $I_{\text{NaP}}$ ) is significant during gradual depolarizations preceding action potentials, especially during burst firing (Del Negro et al., 2010; Taddese & Bean, 2002). In these cases, there is enough time for the onset of inhibition, and the inhibition remains effective until the membrane becomes hyperpolarized for a sufficient time.

An upregulation of the persistent sodium current has been shown to be involved in a number of pathologies, including epilepsies (Oyler et al., 2018; Stafstrom, 2007), cardiac pathologies (Antzelevitch et al., 2014; Chadda et al., 2017; Makielski, 2016), neurodegenerative disorders (van Zundert et al., 2012; Waxman, 2008), pain disorders (Lampert et al., 2006; Misawa et al., 2009; Xie et al., 2011), even cancer metastasis (Djamgoz & Onkal, 2013), and type II diabetes (Rizzetto et al., 2015). Selective inhibitors of  $I_{\text{NaP}}$ , including riluzole, have been found to be effective in cardiac diseases (Antzelevitch et al., 2014; Belardinelli et al., 2013; Karagueuzian et al., 2017), epilepsies (Anderson et al., 2014), pain syndromes (Xie et al., 2011), and neurodegenerative diseases. Riluzole was especially effective in preventing damage in spinal cord and peripheral nerve injury (Fehlings et al., 2016; Ghayour et al., 2017; Głowiczki et al., 2017).

Riluzole represents a new class among  $I_{\text{NaP}}$  selective inhibitors because the non-blocking modulation mechanism endows it with an "ultrafast" offset kinetics, which, however, is not based on actual dissociation. A similar mechanism has been assumed for inhibition by riluzole in a recent computational study (Phillips & Rubin, 2019). To illustrate how this compares to offset kinetics of other well-known sodium channel inhibitors, we re-plotted the data from a comparative study of nine inhibitor compounds (El-Bizri et al., 2018), which included six antiarrhythmic drugs, and the three best known  $I_{\text{NaP}}$  selective inhibitors. We supplemented these data with our results on the effects of riluzole (Fig. 8). Binding rate constants were plotted against unbinding rate constants. The latter were calculated from the time constants of the offset ( $\kappa_{\text{off}} = 1 / \tau_{\text{off}}$ ), then the former was calculated from  $k_{\text{off}}$  and the  $IC_{50}$  value ( $k_{\text{on}} = k_{\text{off}} / IC_{50}$ ). We calculated  $k_{\text{on}}$  and  $k_{\text{off}}$  values the same way for riluzole using time constants of both the fast and slow recovery processes ( $\tau_{\text{fast}} = 2.25$  ms, and  $\tau_{\text{slow}} = 823$  ms), and the  $IC_{50}$  value 3.98  $\mu\text{M}$ . As for the slow recovery process (which reflects true dissociation) riluzole did not differ from the other compounds, but when we used data from fast recovery process, it was in a completely different range. It seems that by staying in the fenestration, riluzole can "pretend" to have been dissociated, which practically increases its speed 366-fold. This allows it to be effective in frequency ranges that are unavailable for conventional drugs. If there was genuine dissociation during the fast recovery process, the value of  $k_{\text{on}}$  would be  $112 \text{ s}^{-1} \mu\text{M}^{-1}$ . This would require an onset time constant of 0.086 ms at 100  $\mu\text{M}$  concentration (from the equation  $\tau_{\text{ov}} = 1 / (cc * k_{\text{on}} + k_{\text{off}})$ ), which is clearly much faster than the experimentally observed onset.

In summary, our data indicate that riluzole is unique in being able to combine fast onset kinetics with high affinity to the conventional local anesthetic binding site of sodium channels. This high-affinity binding occurs only in depolarized (open or inactivated) conformations. The binding itself does not prevent conduction, only slightly alters the gating of channels, making them more likely to stay in inactivated conformation. This produces a preferential inhibition of i)  $I_{\text{NaP}}$ , ii) cells with depolarized membrane potential, and iii) cells firing at high frequencies. The combination of increased persistent component, compromised ability to keep resting membrane potential, and abnormally high firing frequency almost always signifies pathology, which is the reason why riluzole can selectively inhibit this type of pathological activity. The basis of this selectivity is the non-blocking modulation mechanism. We anticipate that compounds of this class (fast-acting non-blocking modulators) may be favorable for the treatment of a number of pathologies, such as neuropathic

pain syndromes, certain neuromuscular diseases, epilepsies, and cardiac fibrillations, which are characterized by an enlarged persistent sodium current and high-frequency firing.

## AUTHOR CONTRIBUTIONS

AM-C, LP, MCF and M.A. designed research; PK performed manual patch-clamp experiments; MCF, LP, and AVT performed photolabeling-coupled electrophysiology experiments; HT performed molecular docking experiments; AM-C, LP, and KZ contributed to the methodology and provided resources; MCF, PK, LP, HT, and AM analyzed data; MCF, LP, HT, and AM wrote the manuscript; all authors have read and approved the manuscript.

## DECLARATION OF TRANSPARENCY AND SCIENTIFIC RIGOUR

This Declaration acknowledges that this paper adheres to the principles for transparent reporting and scientific rigour of preclinical research as stated in the BJP guidelines for Design & Analysis, and as recommended by funding agencies, publishers and other organisations engaged with supporting research.

## ORCID

Tamás Hegedűs <https://orcid.org/0000-0002-0331-9629>

András Málnási-Csizmadia <https://orcid.org/0000-0002-2430-8398>

Arpad Mike <https://orcid.org/0000-0002-9095-8161>

## REFERENCES

- Ahern, C. A., Eastwood, A. L., Dougherty, D. A., & Horn, R. (2008). Electrostatic contributions of aromatic residues in the local anesthetic receptor of voltage-gated sodium channels. *Circulation Research* ,102 (1), 86–94. <https://doi.org/10.1161/CIRCRESAHA.107.160663>
- Alexander, S. P. H., Mathie, A., Peters, J. A., Veale, E. L., Striessnig, J., Kelly, E., Armstrong, J. F., Faccenda, E., Harding, S. D., Pawson, A. J., Sharman, J. L., Southan, C., Davies, J. A., & CGTP Collaborators. (2019). THE CONCISE GUIDE TO PHARMACOLOGY 2019/20: Ion channels. *British Journal of Pharmacology* , 176 Suppl 1 , S142–S228. <https://doi.org/10.1111/bph.14749>
- Anderson, L. L., Thompson, C. H., Hawkins, N. A., Nath, R. D., Petersohn, A. A., Rajamani, S., Bush, W. S., Frankel, W. N., Vanoye, C. G., Kearney, J. A., & George, A. L. (2014). Antiepileptic activity of preferential inhibitors of persistent sodium current. *Epilepsia* ,55 (8), 1274–1283. <https://doi.org/10.1111/epi.12657>
- Antzelevitch, C., Nesterenko, V., Shryock, J. C., Rajamani, S., Song, Y., & Belardinelli, L. (2014). The Role of Late I Na in Development of Cardiac Arrhythmias. In P. C. Ruben (Ed.), *Voltage Gated Sodium Channels* (Vol. 221, pp. 137–168). Springer Berlin Heidelberg. [https://doi.org/10.1007/978-3-642-41588-3\\_7](https://doi.org/10.1007/978-3-642-41588-3_7)
- Arcisio-Miranda, M., Muroi, Y., Chowdhury, S., & Chanda, B. (2010). Molecular mechanism of allosteric modification of voltage-dependent sodium channels by local anesthetics. *The Journal of General Physiology* , 136 (5), 541–554. <https://doi.org/10.1085/jgp.201010438>
- Armstrong, J. F., Faccenda, E., Harding, S. D., Pawson, A. J., Southan, C., Sharman, J. L., Campo, B., Cavanagh, D. R., Alexander, S. P. H., Davenport, A. P., Spedding, M., Davies, J. A., & NC-IUPHAR. (2019). The IUPHAR/BPS Guide to PHARMACOLOGY in 2020: Extending immunopharmacology content and introducing the IUPHAR/MMV Guide to MALARIA PHARMACOLOGY. *Nucleic Acids Research* . <https://doi.org/10.1093/nar/gkz951>
- Belardinelli, L., Liu, G., Smith-Maxwell, C., Wang, W.-Q., El-Bizri, N., Hirakawa, R., Karpinski, S., Hong Li, C., Hu, L., Li, X.-J., Crumb, W., Wu, L., Koltun, D., Zablocki, J., Yao, L., Dhalla, A. K., Rajamani, S., & Shryock, J. C. (2013). A Novel, Potent, and Selective Inhibitor of Cardiac Late Sodium Current Suppresses Experimental Arrhythmias. *Journal of Pharmacology and Experimental Therapeutics* ,344 (1), 23–32. <https://doi.org/10.1124/jpet.112.198887>

- Boiteux, C., Vorobyov, I., French, R. J., French, C., Yarov-Yarovoy, V., & Allen, T. W. (2014). Local anesthetic and antiepileptic drug access and binding to a bacterial voltage-gated sodium channel. *Proceedings of the National Academy of Sciences of the United States of America* , 111 (36), 13057–13062. <https://doi.org/10.1073/pnas.1408710111>
- Buyan, A., Sun, D., & Corry, B. (2018). Protonation state of inhibitors determines interaction sites within voltage-gated sodium channels. *Proceedings of the National Academy of Sciences of the United States of America* , 115 (14), E3135–E3144. <https://doi.org/10.1073/pnas.1714131115>
- Cannon, S. C. (2018). Sodium Channelopathies of Skeletal Muscle. *Handbook of Experimental Pharmacology* , 246 , 309–330. [https://doi.org/10.1007/164\\_2017\\_52](https://doi.org/10.1007/164_2017_52)
- Catterall, W. A., Lenaeus, M. J., & El-Din, T. M. G. (2019). Structure and Pharmacology of Voltage-Gated Sodium and Calcium Channels. *Annual Review of Pharmacology and Toxicology* . <https://doi.org/10.1146/annurev-pharmtox-010818-021757>
- Chadda, K. R., Jeevaratnam, K., Lei, M., & Huang, C. L.-H. (2017). Sodium channel biophysics, late sodium current and genetic arrhythmic syndromes. *Pflügers Archiv - European Journal of Physiology* , 469 (5–6), 629–641. <https://doi.org/10.1007/s00424-017-1959-1>
- Curtis, M. J., Alexander, S., Cirino, G., Docherty, J. R., George, C. H., Giembycz, M. A., Hoyer, D., Insel, P. A., Izzo, A. A., Ji, Y., MacEwan, D. J., Sobey, C. G., Stanford, S. C., Teixeira, M. M., Wonnacott, S., & Ahluwalia, A. (2018). Experimental design and analysis and their reporting II: Updated and simplified guidance for authors and peer reviewers: Editorial. *British Journal of Pharmacology* , 175 (7), 987–993. <https://doi.org/10.1111/bph.14153>
- Del Negro, C. A., Hayes, J. A., Pace, R. W., Brush, B. R., Teruyama, R., & Feldman, J. L. (2010). Synaptically activated burst-generating conductances may underlie a group-pacemaker mechanism for respiratory rhythm generation in mammals. In *Progress in Brain Research* (Vol. 187, pp. 111–136). Elsevier. <https://doi.org/10.1016/B978-0-444-53613-6.00008-3>
- Djamgoz, M. B. A., & Onkal, R. (2013). Persistent current blockers of voltage-gated sodium channels: A clinical opportunity for controlling metastatic disease. *Recent Patents on Anti-Cancer Drug Discovery* , 8 (1), 66–84. <https://doi.org/10.2174/15748928130107>
- El-Bizri, N., Xie, C., Liu, L., Limberis, J., Krause, M., Hirakawa, R., Nguyen, S., Tabuena, D. R., Belardinelli, L., & Kahlig, K. M. (2018). Eleclazine exhibits enhanced selectivity for long QT syndrome type 3-associated late Na<sup>+</sup> current. *Heart Rhythm* , 15 (2), 277–286. <https://doi.org/10.1016/j.hrthm.2017.09.028>
- Fehlings, M. G., Nakashima, H., Nagoshi, N., Chow, D. S. L., Grossman, R. G., & Kopjar, B. (2016). Rationale, design and critical end points for the Riluzole in Acute Spinal Cord Injury Study (RISCIS): A randomized, double-blinded, placebo-controlled parallel multi-center trial. *Spinal Cord* , 54 (1), 8–15. <https://doi.org/10.1038/sc.2015.95>
- Fischer, B. D., Ho, C., Kuzin, I., Bottaro, A., & O’Leary, M. E. (2017). Chronic exposure to tumor necrosis factor in vivo induces hyperalgesia, upregulates sodium channel gene expression and alters the cellular electrophysiology of dorsal root ganglion neurons. *Neuroscience Letters* , 653 , 195–201. <https://doi.org/10.1016/j.neulet.2017.05.004>
- Franke, C., Hatt, H., & Dudel, J. (1987). Liquid filament switch for ultra-fast exchanges of solutions at excised patches of synaptic membrane of crayfish muscle. *Neuroscience Letters* , 77 (2), 199–204. [https://doi.org/10.1016/0304-3940\(87\)90586-6](https://doi.org/10.1016/0304-3940(87)90586-6)
- Ghayour, M. B., Abdolmaleki, A., & Behnam-Rassouli, M. (2017). The effect of Riluzole on functional recovery of locomotion in the rat sciatic nerve crush model. *European Journal of Trauma and Emergency Surgery* , 43 (5), 691–699. <https://doi.org/10.1007/s00068-016-0691-4>

- Gloviczki, B., Török, D. G., Márton, G., Gál, L., Bodzay, T., Pintér, S., & Nógrádi, A. (2017). Delayed Spinal Cord–Brachial Plexus Reconnection after C7 Ventral Root Avulsion: The Effect of Reinnervating Motoneurons Rescued by Riluzole Treatment. *Journal of Neurotrauma* , *34* (15), 2364–2374. <https://doi.org/10.1089/neu.2016.4754>
- Hammarström, A., & Gage, P. (2002). Hypoxia and persistent sodium current. *European Biophysics Journal* , *31* (5), 323–330. <https://doi.org/10.1007/s00249-002-0218-2>
- Hanck, D. A., Makielski, J. C., & Sheets, M. F. (1994). Kinetic effects of quaternary lidocaine block of cardiac sodium channels: A gating current study. *The Journal of General Physiology* , *103* (1), 19–43.
- Hanck, Dorothy A., Nikitina, E., McNulty, M. M., Fozzard, H. A., Lipkind, G. M., & Sheets, M. F. (2009). Using lidocaine and benzocaine to link sodium channel molecular conformations to state-dependent antiarrhythmic drug affinity. *Circulation Research* , *105* (5), 492–499. <https://doi.org/10.1161/CIRCRESAHA.109.198572>
- Hille, B. (1977). Local anesthetics: Hydrophilic and hydrophobic pathways for the drug-receptor reaction. *The Journal of General Physiology* , *69* (4), 497–515.
- Jonas, P. (1995). Fast Application of Agonists to Isolated Membrane Patches. In B. Sakmann & E. Neher (Eds.), *Single-Channel Recording* (pp. 231–243). Springer US. [https://doi.org/10.1007/978-1-4419-1229-9\\_10](https://doi.org/10.1007/978-1-4419-1229-9_10)
- Karagueuzian, H. S., Pezhouman, A., Angelini, M., & Olcese, R. (2017). Enhanced Late Na and Ca Currents as Effective Antiarrhythmic Drug Targets. *Frontiers in Pharmacology* , *8* . <https://doi.org/10.3389/fphar.2017.00036>
- Lampert, A., Hains, B. C., & Waxman, S. G. (2006). Upregulation of persistent and ramp sodium current in dorsal horn neurons after spinal cord injury. *Experimental Brain Research* , *174* (4), 660–666. <https://doi.org/10.1007/s00221-006-0511-x>
- Liu, H., Atkins, J., & Kass, R. S. (2003). Common molecular determinants of flecainide and lidocaine block of heart Na<sup>+</sup> channels: Evidence from experiments with neutral and quaternary flecainide analogues. *The Journal of General Physiology* , *121* (3), 199–214. <https://doi.org/10.1085/jgp.20028723>
- Lukacs, P., Földi, M. C., Valánszki, L., Casanova, E., Biri-Kovács, B., Nyitray, L., Málnási-Csizmadia, A., & Mike, A. (2018). Non-blocking modulation contributes to sodium channel inhibition by a covalently attached photoreactive riluzole analog. *Scientific Reports* , *8* (1), 8110. <https://doi.org/10.1038/s41598-018-26444-y>
- Ma, C., Greenquist, K. W., & LaMotte, R. H. (2006). Inflammatory Mediators Enhance the Excitability of Chronically Compressed Dorsal Root Ganglion Neurons. *Journal of Neurophysiology* , *95* (4), 2098–2107. <https://doi.org/10.1152/jn.00748.2005>
- Makielski, J. C. (2016). Late sodium current: A mechanism for angina, heart failure, and arrhythmia. *Trends in Cardiovascular Medicine* , *26* (2), 115–122. <https://doi.org/10.1016/j.tcm.2015.05.006>
- Martin, L. J., & Corry, B. (2014). Locating the route of entry and binding sites of benzocaine and phenytoin in a bacterial voltage gated sodium channel. *PLoS Computational Biology* , *10* (7), e1003688. <https://doi.org/10.1371/journal.pcbi.1003688>
- Meisler, M. H. (2019). SCN8A encephalopathy: Mechanisms and models. *Epilepsia* , *60 Suppl 3* , S86–S91. <https://doi.org/10.1111/epi.14703>
- Mike, A., & Lukacs, P. (2010). The enigmatic drug binding site for sodium channel inhibitors. *Current Molecular Pharmacology* , *3* (3), 129–144. <https://doi.org/10.2174/1874467211003030129>
- Misawa, S., Sakurai, K., Shibuya, K., Isole, S., Kanai, K., Ogino, J., Ishikawa, K., & Kuwabara, S. (2009). Neuropathic pain is associated with increased nodal persistent Na<sup>+</sup> currents in human diabetic neuropathy. *Journal of the Peripheral Nervous System* , *14* (4), 279–284. <https://doi.org/10.1111/j.1529-8027.2009.00239.x>

- Morris, C. E., & Joos, B. (2016). Nav Channels in Damaged Membranes. *Current Topics in Membranes* , 78 , 561–597. <https://doi.org/10.1016/bs.ctm.2016.06.001>
- Muroi, Y., & Chanda, B. (2009). Local anesthetics disrupt energetic coupling between the voltage-sensing segments of a sodium channel. *The Journal of General Physiology* , 133 (1), 1–15. <https://doi.org/10.1085/jgp.200810103>
- Nguyen, P. T., DeMarco, K. R., Vorobyov, I., Clancy, C. E., & Yarov-Yarovoy, V. (2019). Structural basis for antiarrhythmic drug interactions with the human cardiac sodium channel. *Proceedings of the National Academy of Sciences of the United States of America* , 116 (8), 2945–2954. <https://doi.org/10.1073/pnas.1817446116>
- Oyryer, J., Maljevic, S., Scheffer, I. E., Berkovic, S. F., Petrou, S., & Reid, C. A. (2018). Ion Channels in Genetic Epilepsy: From Genes and Mechanisms to Disease-Targeted Therapies. *Pharmacological Reviews* , 70 (1), 142–173. <https://doi.org/10.1124/pr.117.014456>
- Pesti, K., Szabo, A. K., Mike, A., & Vizi, E. S. (2014). Kinetic properties and open probability of  $\alpha 7$  nicotinic acetylcholine receptors. *Neuropharmacology* , 81 , 101–115. <https://doi.org/10.1016/j.neuropharm.2014.01.034>
- Phillips, R. S., & Rubin, J. E. (2019). Effects of persistent sodium current blockade in respiratory circuits depend on the pharmacological mechanism of action and network dynamics. *PLOS Computational Biology* , 15 (8), e1006938. <https://doi.org/10.1371/journal.pcbi.1006938>
- Raju, S. G., Barber, A. F., LeBard, D. N., Klein, M. L., & Carnevale, V. (2013). Exploring volatile general anesthetic binding to a closed membrane-bound bacterial voltage-gated sodium channel via computation. *PLoS Computational Biology* , 9 (6), e1003090. <https://doi.org/10.1371/journal.pcbi.1003090>
- Rizzetto, R., Rocchetti, M., Sala, L., Ronchi, C., Villa, A., Ferrandi, M., Molinari, I., Bertuzzi, F., & Zaza, A. (2015). Late sodium current (INaL) in pancreatic  $\beta$ -cells. *Pflügers Archiv - European Journal of Physiology* , 467 (8), 1757–1768. <https://doi.org/10.1007/s00424-014-1613-0>
- Rogawski, M. A., & Löscher, W. (2004). The neurobiology of antiepileptic drugs for the treatment of nonepileptic conditions. *Nature Medicine* , 10 (7), 685–692. <https://doi.org/10.1038/nm1074>
- Seeliger, D., & de Groot, B. L. (2010). Ligand docking and binding site analysis with PyMOL and AutoDock/Vina. *Journal of Computer-Aided Molecular Design* , 24 (5), 417–422. <https://doi.org/10.1007/s10822-010-9352-6>
- Stafstrom, C. E. (2007). Persistent sodium current and its role in epilepsy. *Epilepsy Currents* , 7 (1), 15–22. <https://doi.org/10.1111/j.1535-7511.2007.00156.x>
- Taddese, A., & Bean, B. P. (2002). Subthreshold Sodium Current from Rapidly Inactivating Sodium Channels Drives Spontaneous Firing of Tuberomammillary Neurons. *Neuron* , 33 (4), 587–600. [https://doi.org/10.1016/S0896-6273\(02\)00574-3](https://doi.org/10.1016/S0896-6273(02)00574-3)
- Tang, Z., Chen, Z., Tang, B., & Jiang, H. (2015). Primary erythromelalgia: A review. *Orphanet Journal of Rare Diseases* , 10 , 127. <https://doi.org/10.1186/s13023-015-0347-1>
- Trott, O., & Olson, A. J. (2010). AutoDock Vina: Improving the speed and accuracy of docking with a new scoring function, efficient optimization, and multithreading. *Journal of Computational Chemistry* , 31 (2), 455–461. <https://doi.org/10.1002/jcc.21334>
- van Zundert, B., Izaurieta, P., Fritz, E., & Alvarez, F. J. (2012). Early pathogenesis in the adult-onset neurodegenerative disease amyotrophic lateral sclerosis. *Journal of Cellular Biochemistry* , 113 (11), 3301–3312. <https://doi.org/10.1002/jcb.24234>
- Wang, Y., Yang, E., Wells, M. M., Bondarenko, V., Woll, K., Carnevale, V., Granata, D., Klein, M. L., Eckenhoff, R. G., Dailey, W. P., Covarrubias, M., Tang, P., & Xu, Y. (2018). Propofol inhibits the voltage-

gated sodium channel NaChBac at multiple sites. *The Journal of General Physiology* , 150 (9), 1317–1331. <https://doi.org/10.1085/jgp.201811993>

Waxman, S. G. (2008). Mechanisms of Disease: Sodium channels and neuroprotection in multiple sclerosis—current status. *Nature Clinical Practice Neurology* , 4 (3), 159–169. <https://doi.org/10.1038/ncpneuro0735>

Xie, R.-G., Zheng, D.-W., Xing, J.-L., Zhang, X.-J., Song, Y., Xie, Y.-B., Kuang, F., Dong, H., You, S.-W., Xu, H., & Hu, S.-J. (2011). Blockade of Persistent Sodium Currents Contributes to the Riluzole-Induced Inhibition of Spontaneous Activity and Oscillations in Injured DRG Neurons. *PLoS ONE* , 6 (4), e18681. <https://doi.org/10.1371/journal.pone.0018681>

Zhang, H., Zou, B., Du, F., Xu, K., & Li, M. (2015). Reporting sodium channel activity using calcium flux: Pharmacological promiscuity of cardiac Nav1.5. *Molecular Pharmacology* , 87 (2), 207–217. <https://doi.org/10.1124/mol.114.094789>

Zhang, Q., Ma, J.-H., Li, H., Wei, X.-H., Zheng, J., Li, G., Wang, C.-Y., Wu, Y., He, Q.-H., & Wu, L. (2019). Increase in CO<sub>2</sub> levels by upregulating late sodium current is proarrhythmic in the heart. *Heart Rhythm* , 16 (7), 1098–1106. <https://doi.org/10.1016/j.hrthm.2019.01.029>

Zheng, Q., Fang, D., Cai, J., Wan, Y., Han, J.-S., & Xing, G.-G. (2012). Enhanced Excitability of Small Dorsal Root Ganglion Neurons in Rats with Bone Cancer Pain. *Molecular Pain* , 8 , 1744-8069-8–24. <https://doi.org/10.1186/1744-8069-8-24>

## FIGURE LEGENDS

**Φιγ. 1. Ρεσοερψ φρομ ιναςτιατιον ιν τηε αβσενζε ανδ πρεσενζε οφ 100 μM ριλυζολε ιν ΩΤ ζηαννελς.** The RFI protocol is shown in the upper panel. The duration of the hyperpolarizing gap between the two depolarizations is progressively increased. Peak amplitudes of the 2nd pulse-evoked currents are plotted against hyperpolarizing gap duration. Thin black lines – normalized control amplitudes in n = 9 cells, thin red lines – amplitudes in the same 9 cells in the presence of 100 μM riluzole. The effect of riluzole in each cell was normalized to the control in the same cell. Averaging (thick lines) was performed as described in Methods.

**Fig. 2. Effect of riluzole perfusion as monitored with the 3PT protocol on WT channels. A** The voltage protocol. Blue, red, and green color indicate 1<sup>st</sup>, 2<sup>nd</sup>, and 3<sup>rd</sup> depolarizations, respectively, as in panels D to F.

**B** Example of sodium currents evoked in a typical WT channel expressing cell by the three depolarizations of the 3PT protocol. Subsequent traces are overlaid on each other. Blue traces show control, dark to light red show successive traces during riluzole application, light gray to black traces show successive traces during washout.

**C** The same currents after subtraction of capacitive and leakage artifacts.

**D** Illustration of the first 29 consecutive trains (protocol in the upper panel), and the currents evoked by them (lower panel). Peaks of 1<sup>st</sup>, 2<sup>nd</sup>, and 3<sup>rd</sup> pulse-evoked currents are marked with blue, red, and green circles, respectively. Shaded area indicates the perfusion of 100 μM riluzole.

**E** Amplitude plots for 7 individual cells. Connecting peak amplitudes of 1<sup>st</sup> (blue), 2<sup>nd</sup> (red), or 3<sup>rd</sup> (green) pulse-evoked currents gives a plot of peak amplitudes throughout the whole experiment. To help compare the extent of inhibition, 1<sup>st</sup>, 2<sup>nd</sup>, and 3<sup>rd</sup> pulse-evoked currents were normalized each to its own control (peak amplitudes recorded during the first train).

**F** Onset and offset time constants (mean ± SEM) for the amplitude plots of the seven cells shown in panel E. Data from one individual cell (the same as in panels B to D) are shown for illustration. Mono- or bi-exponential functions were fitted to traces after correcting for slow inactivation (see Methods). Dashed lines show exponentials fitted to this particular cell.

**Φιγ. 3. Πεσοερψ φρομ ιναστιατιον ιν τηε αβσεινσε ανδ πρεσεινσε οφ 100 μM ριλυζολε ιν Φ1579A μυταντ ζηαννελς.**

Peak amplitudes are plotted against hyperpolarizing gap length. Thin black lines – normalized control data from  $n = 7$  cells, thin red lines – 100 μM riluzole from the same 7 cells, normalized each to the control in the same cell. Averaging (thick lines) was performed as described in Methods.

**Fig. 4. Effect of riluzole perfusion as monitored with the 3PT protocol on F1579A mutant channels.** The voltage protocol is the same as in Fig. 2.

**A** Example of sodium currents evoked in a typical F1579A mutant channel expressing cell by the three depolarizations of the 3PT protocol. Subsequent traces are overlaid on each other. Blue traces show control, dark to light red show successive traces during riluzole application, light gray to black traces show successive traces during washout.

**B** The same currents after subtraction of capacitive and leakage artifacts.

**C** Illustration of the first 29 consecutive trains (protocol in the upper panel), and the currents evoked by them (lower panel). Peaks of 1<sup>st</sup>, 2<sup>nd</sup>, and 3<sup>rd</sup> pulse-evoked currents are marked with blue, red, and green circles, respectively. Shaded area indicates the perfusion of 100 μM riluzole.

**D** Amplitude plots for 9 individual cells. Connecting peak amplitudes of 1<sup>st</sup> (blue), 2<sup>nd</sup> (red), or 3<sup>rd</sup> (green) pulse-evoked currents gives a plot of peak amplitudes throughout the whole experiment. To help compare the extent of inhibition, 1<sup>st</sup>, 2<sup>nd</sup>, and 3<sup>rd</sup> pulse-evoked currents were normalized each to its own control (peak amplitudes recorded during the first train).

**E** Onset and offset time constants (mean ± SEM) for the amplitude plots of the nine cells shown in panel D. Data from one individual cell (the same as in panels A to C) is shown for illustration. Mono- or bi-exponential functions were fitted to traces after correcting for slow inactivation (see Methods). Dashed lines show exponentials fitted to this particular cell.

**Fig. 5. Effect of conformation-selective photolabeling by azido-riluzole on gating kinetics of WT channels.** **A** Experimental protocol. **RFI**, **SSI**, and **SDO** protocols were run before and after azido-riluzole perfusion and pulsed UV illumination. During azido-riluzole perfusion, 90 ms UV illumination pulses were used at a specific time within each cycle (shown by purple shaded areas) in all three voltage protocols.

**B, C, D** Assessment of gating kinetics and equilibrium before and after azido-riluzole perfusion and UV irradiation. Black lines show control data before azido-riluzole perfusion and UV illumination, colored lines show data measured after stopping UV pulses and washing out azido-riluzole. Blue lines: after resting-state-illumination protocol; teal lines: after V-half-illumination protocol; green lines: after inactivated-state-illumination protocol. Amplitudes were normalized to the maximal amplitude in control. Insets: Amplitudes normalized each to its own maxima. **B**: Plot of 2<sup>nd</sup> pulse-evoked peak amplitudes (mean ± SEM) against hyperpolarizing gap duration. **C**: Plot of channel availability against pre-pulse potential. **D**: Plot of 2<sup>nd</sup> pulse-evoked amplitudes against 1<sup>st</sup> pulse duration.

**Fig. 6. Effect of conformation-selective photolabeling by azido-riluzole on gating kinetics of F1579A mutant channels.**

**A, B, C** Assessment of gating kinetics and equilibrium before and after azido-riluzole perfusion and UV irradiation. Protocols and color of lines are the same as in Fig. 5: Control (black), after resting-state-illumination (blue); after V-half-illumination (teal); after inactivated-state-illumination (green). Amplitudes were normalized to the maximal amplitude in control. Insets: Amplitudes normalized each to its own maxima.

**Fig. 7. Riluzole does not block the pore.** Riluzole was docked into the structural model of human Nav1.4 (PDB ID: 6AGF) (**A**) and its F1586A mutant (**B**). Gray sticks: best poses of riluzole; sticks and balls: F436 (teal), F1284 (blue), and F1586 (red); green, cyan, orange, and marine: domains I, II, III, and IV.

### Fig. 8. Kinetics of riluzole in comparison to other sodium channel inhibitor compounds.

Calculated binding and unbinding rates of riluzole to 9 sodium channel inhibitor compounds. The figure was re-plotted from El-Bizri et al., (2018)., and supplemented with our data with riluzole, in which case we calculated binding and unbinding rates for both the fast and the slow recovery processes. (AMD – amiodarone; ELEC – eleclazine; FLC – flecainide; LID – lidocaine; MEX – mexiletine; PRF – propafenone; QUI – quinidine; RIL – riluzole).

Fig. 1

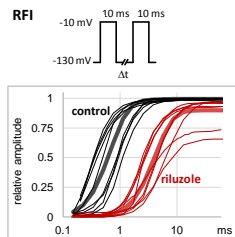
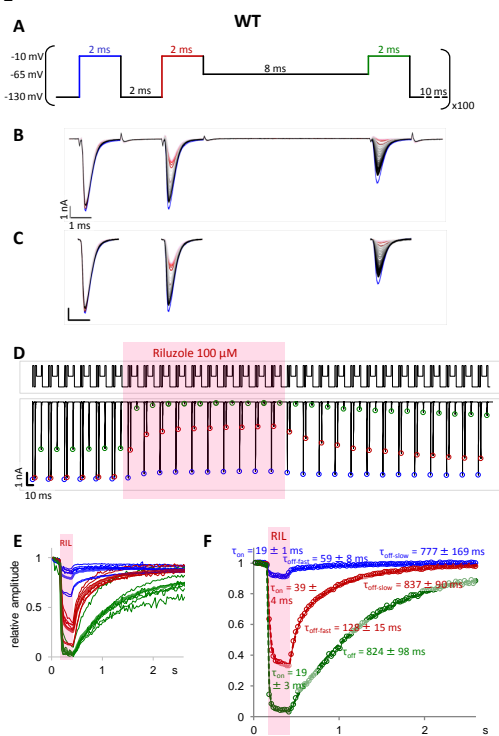


Fig. 2



**Fig. 3**

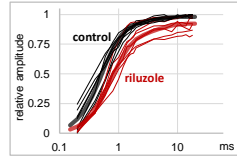


Fig. 4

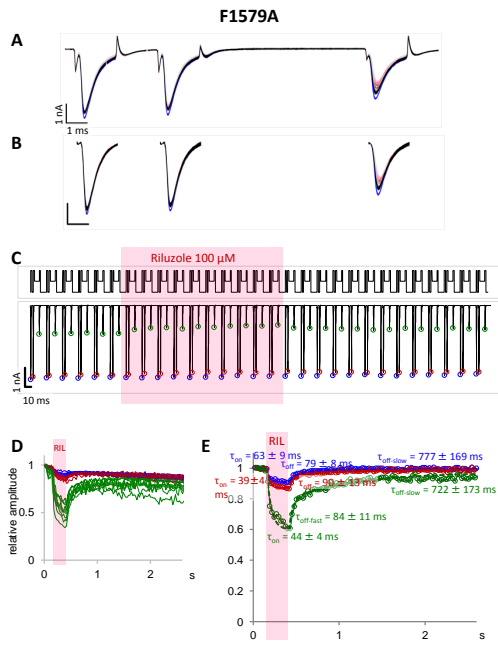


Fig. 5

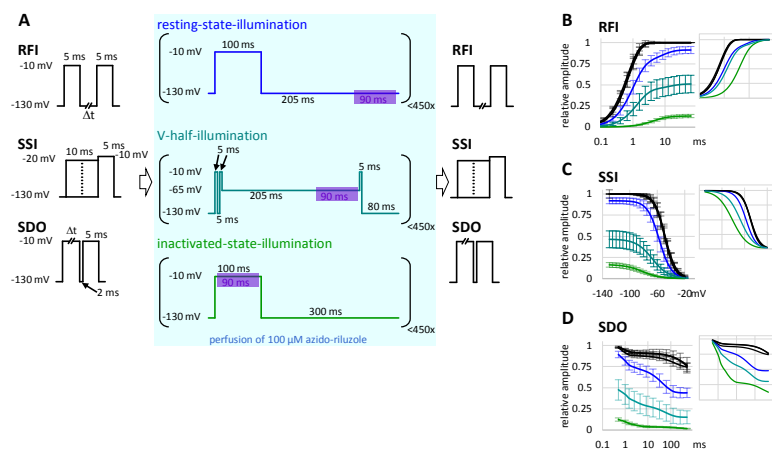
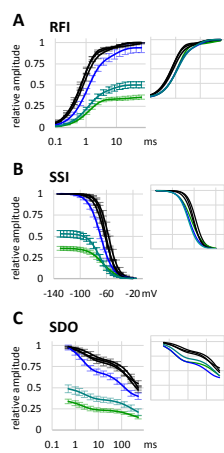


Fig. 6



**Fig. 7**

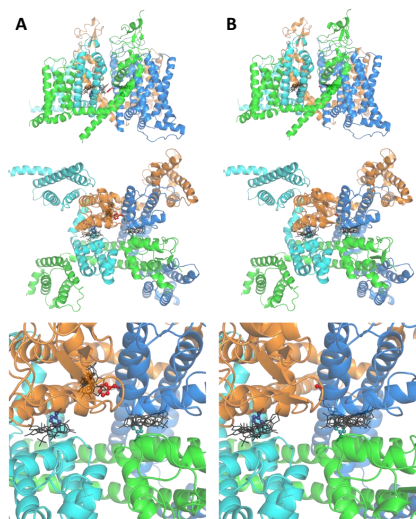


Fig. 8

